

Universal Time Variations in Space Weather

Michael Lockwood¹, Mathew J Owens¹, Carl Haines¹, Luke Barnard¹, Christopher John Scott¹, Aude Chambodut², Kathryn A McWilliams³, and Alan W P Thomson⁴

¹University of Reading

²EOST/UDS

³University of Saskatchewan

⁴British Geological Survey

November 21, 2022

Abstract

We introduce the inductive effects of polar cap motions towards and away from the Sun into magnetospheric electrodynamics and show how this explains observed Universal Time variations in hemispheric geomagnetic indices. The large (and growing) hemispheric asymmetry in the offsets of the geomagnetic (dip or eccentric dipole) poles from Earth's rotational axis means that the effect is not cancelled out in global indices. By adding this effect to that of the Russell-McPherron effect on solar wind-magnetosphere coupling, that of ionospheric conductivities, and that of the solar wind dynamic pressure and dipole tilt on the near-Earth tail lobe field and cross-tail current sheet, we are able to model the persistent “equinoctial” time-of-day/time-of-year pattern (with additional net Universal time variations) observed in the *an*, *as* and *am* geomagnetic indices since 1959. We discuss the implications for the longitudinal dependence of the effects of extreme space weather events

Universal Time Variations in Space Weather

M. Lockwood¹†, M.J. Owens¹, C. Haines¹, L.A. Barnard¹, C.J. Scott¹, A. Chambodut², K.A. McWilliams³ and A.W.P. Thomson⁴

¹ Department of Meteorology, University of Reading, Reading, UK. ² École et Observatoire des Sciences de la Terre, Université de Strasbourg and CNRS, France. ³ Institute of Space and Atmospheric Studies, University of Saskatchewan, Saskatoon, Saskatchewan, Canada. ⁴ British Geological Survey, Edinburgh, UK.

Corresponding author: Mike Lockwood (m.lockwood@reading.ac.uk)

† ORCID number: [0000-0002-7397-2172](https://orcid.org/0000-0002-7397-2172)

Key Points:

- We introduce polar cap motions into magnetospheric dynamics for the first time
- The results explain the Universal Time variations in hemispheric geomagnetic indices
- The “equinoctial” (“McIntosh”) pattern is well explained by the effects of solar wind dynamic pressure and dipole tilt on the near-Earth current sheet.

Estimated length: 3442 words = 6.9 publication units

4 figures = 4.0 publication units

Total = 10.9 publication units

Paper is accompanied by the supplementary materials file [Lockwood_GRL_SuppInfo.pdf](#)

Abstract (142 words)

We introduce the inductive effects of polar cap motions towards and away from the Sun into magnetospheric electrodynamic and show how this explains observed Universal Time variations in hemispheric geomagnetic indices. The large (and growing) hemispheric asymmetry in the offsets of the geomagnetic (dip or eccentric dipole) poles from Earth’s rotational axis means that the effect is not cancelled out in global indices. By adding this effect to that of the Russell-McPherron effect on solar wind-magnetosphere coupling, that of ionospheric conductivities, and that of the solar wind dynamic pressure and dipole tilt on the near-Earth tail lobe field and cross-tail current sheet, we are able to model the persistent “equinoctial” time-of-day/time-of-year pattern (with additional net Universal time variations) observed in the *am*, *an* and *as* geomagnetic indices since 1959. We discuss the implications for the longitudinal dependence of the effects of extreme space weather events.

Plain Language Summary

The Universal Time variation in geomagnetic activity was first noted in 1925 but despite many attempts to explain it, its origin has remained a puzzle. We here introduce a previously overlooked factor, namely the effects of polar cap motions towards and away from the Sun caused by the Earth’s rotation. We show the effect is significant and that, when added to other known effects, it can explain the best observations, which are available for the past 60 years. The results have implications for the design and mitigation of space weather effects on ground-based systems, such as power grids and long pipelines, at different longitudes.

1 Introduction

Two of the longest-surviving puzzles in solar terrestrial physics and space weather have been the “equinoctial” (or “McIntosh”) time-of-year (F) - Universal Time (UT) pattern of geomagnetic activity (McIntosh, 1959; Cliver et al. 2000), and its net UT variation (when averaged over all F), initially detected by Bartels (1925). These are closely linked, via the precessions of Earth’s magnetic axis \vec{M} , to the semi-annual variation, first reported even earlier by Broun (1848), which was explained early in the space age with the highly successful Russell-McPherron (1973) (R-M) paradigm. However, the R-M theory predicts a quite different F - UT pattern and no net UT variation. Despite a very large number of postulated additional mechanisms (see review by Lockwood et al., 2020a) none has been able to explain either anomaly satisfactorily. Some of the proposals invoked modulating dayside solar wind-magnetosphere coupling, but a detailed study of data from the global network of magnetometers unambiguously shows that the equinoctial pattern arises on the nightside of the Earth (Finch et al., 2008; Chambodut et al., 2013, Lockwood et al., 2020a). We here use the “expanding-contracting polar cap” (ECPC) model (Cowley and Lockwood, 1992) to show that the missing factor has been the inductive effects of the diurnal sunward and antisunward velocities of the polar caps caused by Earth’s rotation. On a global scale, this introduces a UT variation because of the hemispheric asymmetry in the geomagnetic field that is now changing faster than at any time since observations began (Thébault et al., 2015).

2 Methods

2.1 Theoretical drivers of F - UT patterns: R-M and equinoctial

The R-M theory is geometric, being based in the facts that the near-Earth interplanetary magnetic field (IMF) is ordered in a solar reference frame (Geocentric Solar Equatorial, GSEQ, where X points from the center of the Earth to the center of the Sun, Y is parallel to the solar equatorial plane and is close to duskward and Z makes up the right hand set and is close to northward) but power input into the magnetosphere, P_{α} , depends on the IMF orientation in the Geocentric Solar Magnetospheric frame (GSM, which has the same X axis but is rotated so that the Z axis lines up with the projection of \vec{M} onto the YZ plane) (see review by Lockwood et al., 2020a). This is because the dominant solar wind-magnetosphere coupling mechanism, magnetic reconnection, depends on the magnetic shear across the dayside magnetopause and hence on the IMF $[B_z]_{GSM}$ component.

The coloured pixels in parts a and b of Figure 1 show the F - UT patterns of average P_{α} , computed from 1-minute interplanetary observations available for 1980-2019 (see review by Lockwood, 2019) for IMF $[B_Y]_{GSEQ} < 0$ and $[B_Y]_{GSEQ} > 0$, respectively, and the black contours are the predictions of the R-M effect. The agreement is very close and the effect is considerable (a $\pm 50\%$ modulation). However, the increase around the March equinox ($F = 0.218$) for $[B_Y]_{GSEQ} > 0$ in Figure 1a is almost cancelled by the decrease for $[B_Y]_{GSEQ} < 0$ and the same near-cancellation occurs for the peak around the September equinox ($F = 0.730$) in Figure 1b (Berthelier, 1976; Lockwood et al., 2020b). This cancellation is much smaller for geomagnetic indices than for P_{α} (Lockwood et al., 2020a; b). Because the distribution of $[B_Y]_{GSEQ}$ is close to being symmetrical about zero, the net R-M effect in P_{α} for all data is much weaker (a $\pm 5\%$ modulation) and much

less clear-cut in all data as shown in Figure 1c. The theoretical pattern of solar wind driving (for all data) is here termed $P_{RM}(F, UT)$. The equinoctial pattern of the “tilt angle” $\psi(F, UT)$, between \vec{M} and the sunward (X) direction, is shown in Figure 1d with its characteristic “hourglass” form.

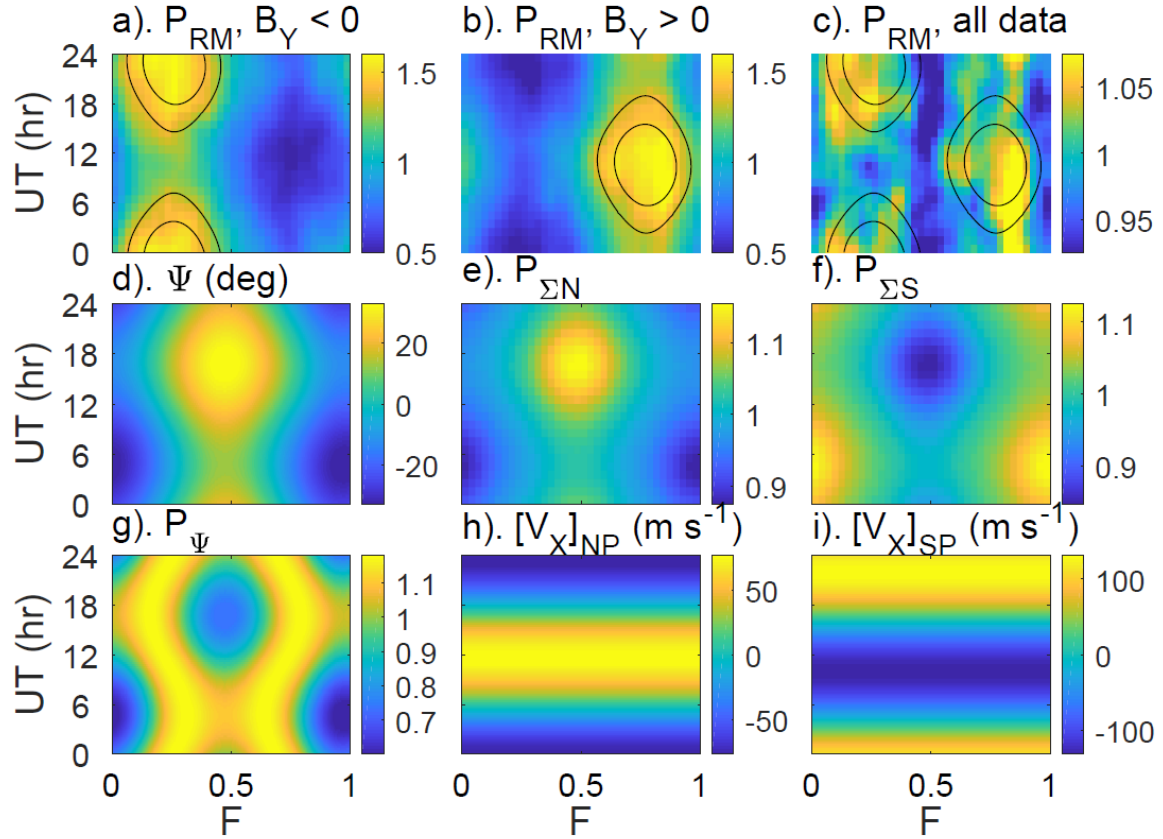


Figure 1. Fraction of year (F) - Universal Time (UT) patterns. Color contoured in (a)-(c) are the power input into the magnetosphere P_α estimated from 1-minute interplanetary observations (available for 1980 onwards) for (a) IMF $[B_Y]_{GSEQ} < 0$; (b) IMF $[B_Y]_{GSEQ} > 0$; and (c) all data. The black lines in (a), (b) and (c) are the best fit theoretical R-M patterns. Other panels are F - UT patterns of: (d) the dipole tilt angle, ψ for the eccentric dipole fit to geomagnetic data in 1989; (e) the northern hemisphere index (an) conductivity factor, $P_{\Sigma N}$; (f) the southern hemisphere index (as) conductivity factor, $P_{\Sigma S}$; (g) the tail squeezing factor P_ψ ; (h) the sunward velocity of the north axial magnetic pole, $[V_X]_{NP}$; (i) the sunward velocity of the south axial magnetic pole, $[V_X]_{SP}$.

2.2 Modelling F - UT patterns in geomagnetic indices

We predict the F - UT patterns of the hemispheric indices an and as (here generically referred to as ans) from the product of 4 terms:

$$ans_m(F, UT) = P_{RM}(F, UT) \cdot P_{\Sigma NS}(F, UT) \cdot P_\psi(F, UT) \cdot [P_{PM}(F, UT)]_{NS} \quad (1)$$

where the terms $P_{\Sigma NS}(F, UT)$, $P_{PM}(F, UT)$ and $P_{\psi}(F, UT)$ and account for the effects of, respectively, ionospheric conductivities, pole motions and dynamic pressure and dipole tilt on the tail lobe, as described in the following subsections. In each case, equations for, and further information on, all terms are given in the supporting information file. We then combine the two modelled hemispheric indices in the same way as for observations:

$$am_m(F, UT) = \{an_m(F, UT) + as_m(F, UT)\}/2 \quad (2)$$

2.3 The ionospheric conductivity terms $P_{\Sigma N}(F, UT)$ and $P_{\Sigma S}(F, UT)$

These terms allow for the effects of ionospheric Hall and Pedersen conductivities generated by photoionization. These both depend on the solar zenith angle (e.g., Ieda et al., 2014) and so, at any fixed geomagnetic location, on the tilt angle ψ . Comparing the observed variations of an and as with time-of-year F yields the functions $P_{\Sigma N}(\psi)$ and $P_{\Sigma S}(\psi)$ hence, from the $\psi(F, UT)$ pattern shown in Figure 1c, $P_{\Sigma N}(F, UT)$ (Figure 1e) and $P_{\Sigma S}(F, UT)$ (Figure 1f).

2.4 The tail squeezing factor $P_{\psi}(F, UT)$

Lockwood et al. (2020b) show that, after the effect of P_{α} is accounted for, the amplitude of the equinoctial pattern in am depends linearly on the solar wind dynamic pressure, p_{SW} , which is known to also increase the magnetic field in the near-Earth tail lobes (and hence the stored magnetic energy and cross-tail current) (Caan et al., 1973), consistent with its squeezing effect on the near-Earth tail (Lockwood, 2013) and its effect on geomagnetic activity (Finch et al., 2008; Lockwood et al., 2020a;b). The factor $P_{\psi}(F, UT)$ shown in Figure 1g is derived from the $\psi(F, UT)$ pattern using the variation $P_{\psi B}(\psi)$, obtained by considering the tail lobe field at a given ψ . This is derived by assuming that the near-Earth geomagnetic tail is in pressure equilibrium and using an empirical model of the locations of the magnetopause. We use a model that includes north-south asymmetries in the magnetopause which therefore includes the effects of hemispheric asymmetry in the geomagnetic field (Lin et al., 2010). To scale this factor we match the amplitude of $P_{\psi B}(F, UT)$ to the equinoctial pattern in am for the mode value of the observed p_{SW} (Lockwood et al., 2020b).

2.5 The effect of pole motions $P_{PM}(F, UT)$

The new factor introduced in this paper arises from the velocity (rather than the location) of the geomagnetic poles in the two hemispheres and has been overlooked until now and is explained by Figure 2. A key part of the highly successful ECPC model of ionospheric convection (Cowley and Lockwood, 1992) is that the interplanetary electric field caused by the flow of solar wind and its embedded magnetic field, the IMF, does not map down the “open” geomagnetic field lines that have been interconnected with the IMF field lines by magnetic reconnection in the dayside magnetopause: only in the case of steady state, which is relatively rare on averaging timescales shorter than the substorm cycle (typically 1-2 hours), does such mapping apply. This is because the normal response of the magnetosphere to the generation of open field lines by magnetopause reconnection (and the consequent power input into the magnetosphere, P_{α}) is the substorm cycle of energy storage and release in the geomagnetic tail.

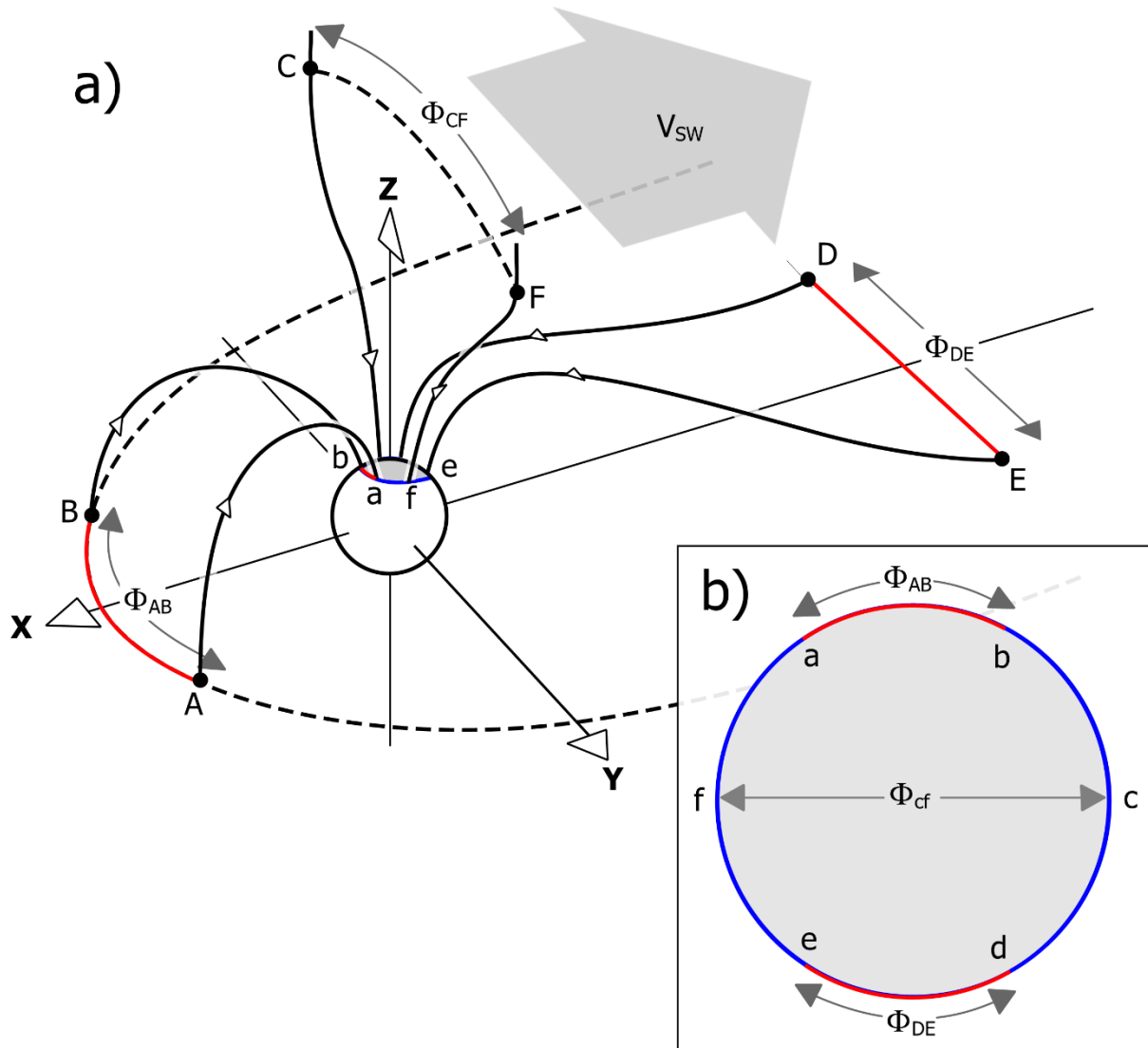


Figure 2. Schematic illustrating inductive decoupling of solar wind and ionospheric electric field and flows that is a key part of the Expanding-Contracting Polar Cap (ECPC) model of non-steady convection. Active reconnection neutral lines and their ionospheric footprints are shown in red. In (a) the X, Y, and Z axes of the Geocentric Solar Magnetospheric frame are shown. The points a, b, c, d, e and f are the ionospheric footprints of the points on the magnetopause or cross tail current sheet A, B, C, D, E and F, respectively. AB is the dayside magnetopause reconnection X-line (across which the voltage Φ_{AB} is applied by the magnetic reconnection that opens field lines) and DE is the reconnection X-line in the cross tail current sheet (where the voltage Φ_{DE} is caused by reconnection that recloses open field lines). CF is the “Stern Gap” (open field lines in interplanetary space that are “frozen”-into the solar wind flow, V_{SW}) that maps to the diameter, cf, of the open polar cap (shown in grey). ABba, DEed and CFfc are all considered here as fixed loops in the GESQ reference frame to which Faraday’s law (in integral form) is applied. (b) shows the northern polar cap viewed in the $-Z$ direction. (after Lockwood and Cowley, 1990 and Lockwood and Morley 2004).

Consider the loop CFfc in Figure 2: we know from the minimum energies of primary precipitating ions and electrons that the field-parallel voltages along Cc and Ff (Φ_{Cc} and Φ_{Ff}) are very small compared to the voltage Φ_{CF} placed by the solar wind flow across the ‘‘Stern gap’’ (the region of open field lines in interplanetary space between C and F), and the transpolar voltage placed across the ionospheric polar cap diameter (cf), Φ_{cf} . Applying Faraday’s law to this loop (in integral form) yields (Lockwood and Cowley, 1990; Lockwood and Morley, 2004)

$$\oint_{CFfc} \vec{E} \cdot d\vec{l} = \Phi_{CF} + \Phi_{Ff} + \Phi_{fc} + \Phi_{Cc} \approx \Phi_{CF} - \Phi_{cf} = -\frac{\partial}{\partial t} \int_{CFfc} \vec{B} \cdot d\vec{A} \quad (3)$$

hence the growth or decay of field threading the loop decouples the voltages Φ_{CF} and Φ_{cf} which is an essential part of the substorm cycle of magnetic energy storage and release in the near-Earth geomagnetic tail. The factor that has previously been overlooked is that the offsets of the magnetic and rotational poles causes the polar caps to undergo a diurnal cycle of sunward and antisunward motion in the GSEQ frame in which the solar wind flow, and hence interplanetary electric field and the voltage Φ_{CF} , are measured. Observations related to the open-closed field line boundary (OCB) show that, at most, 10% of the dipole tilt is reflected in the polar cap location in a geomagnetic frame (Newell and Meng, 1989). This is confirmed by global numerical modelling of the magnetosphere (Kabin et al., 2004) and means that at least 90% of the motions of poles in the GSEQ frame must be reflected in the OCB motions. The effects of these diurnal pole motions have also been seen in the auroral ovals, both in empirical models (Tsyganenko, 2019) and simultaneous whole-oval auroral images of both hemispheres (Stubbs et al., 2005). Fitting an eccentric dipole model to the observed intrinsic geomagnetic field (where the magnetic axis is not forced to pass through the Earth’s center) reveals that the offset from the rotational pole of the southern ‘‘axial’’ magnetic pole is currently roughly twice as large as that for the northern (Koochak and Fraser-Smith, 2017) and hence the amplitude of the sinusoidal sunward velocity in the north, $[V_X]_{NP}$, is roughly half that in the south, $[V_X]_{SP}$. Furthermore, the longitude difference of these poles is not exactly 180° and so these velocities are not quite in antiphase. Transforming pole locations in the geographic frame into the GSEQ frame (we use axial pole positions for the year 1989, at the center of the *am* data period) shows that $[V_X]_{NP}$ and $[V_X]_{SP}$ are almost independent of *F* and their *F-UT* patterns are shown in Figures 1h and 1i, respectively. When a polar cap is moving antisunward/sunward it effectively increases/reduces the voltage applied by the antisunward solar wind flow to the polar cap that hemisphere but also increases/reduces the energy stored in that tail lobe. Because the motions are close to being in antiphase, the energy in one tail lobe grows while the other declines but because of the hemispheric asymmetry in the geomagnetic field, these *UT* variations do not cancel. The effect is significant. The ionospheric magnetic field normal to the *X* direction B_{YZ} averages about 4.5×10^{-5} T over the polar cap, so 90% of the peak V_{SP} of about 120 ms^{-1} is an ionospheric electric field in the GSEQ frame of $0.9V_{SP}B_{YZ} \approx 5 \text{ mVm}^{-1}$; integrating this up over a polar cap of angular radius of 15° (a diameter of about 3500 km, roughly consistent with a value of $\Phi_{cf} = 39$ kV used below) gives a peak voltage modulation of $\Delta\Phi_{cf} = \pm 17$ kV and ± 8.8 kV for the southern and northern polar caps which are not negligible fractions of typical transpolar voltages Φ_{cf} (which vary between about 20kV and 180 kV). Note that the pole velocities are zero at minimum and peak displacement towards the Sun and so *UT* variations due to pole velocities and conductivity are in quadrature.

The only remaining requirement is to scale the hemispheric factors $P_{PM}(F, UT)$ that quantify the effect of the pole motions on the an and as indices. As noted above, the fractional effect depends on the transpolar voltage Φ_{cf} . Taking the mean am over the entire interval 1950-2019 of 21 nT and the regression given by Lockwood et al. (2020b) we get an average Φ_{cf} of 39 kV, for which the peak effect in the southern polar cap is $\Delta\Phi_{cf}/\Phi_{cf} \sim 17/39 = 0.44$: i.e., a $\pm 44\%$ modulation. That in the northern hemisphere is a $\pm 22.5\%$ modulation. In theory, this effect could modulate energy stored in the tail on a diurnal timescale without altering the field-aligned currents and the geomagnetic indices or it could be fully reflected in the indices. This gives rise to the one free fit parameter in our model c_{PM} that is the ratio of the induced fractional variation in the hemispheric index to the ratio $\Delta\Phi_{cf}/\Phi_{cf}$ and which is between 0 and 1.

3 Data Used

In Figures 1a-1c we use 1-minute data on the solar wind and interplanetary magnetic field made available from 1980 onwards in the Omni2 dataset to estimate the power input into the magnetosphere P_α (see supporting information). Data gaps are handled using the criteria for the required number of samples for each parameter that ensures that the error in hourly P_α values is below 5%. These criteria were established by Lockwood et al (2019a) by introducing synthetic data gaps into almost continuous data.

The am geomagnetic index (Mayaud, 1980), and its north and south hemisphere components, an and as , is by far the best to use in this context because it employs the most uniform network of stations in both hemispheres and is compiled using an algorithm that has been shown to give an almost constant response to solar wind forcing in both F and UT . Lockwood et al. (2019b) show that for low am (< 20 nT) the F - UT patterns of response of the an and as indices to solar wind

forcing are constant to within 2% and the deviations largely cancel, such that the am response is constant to within 0.5%. For high am (>60 nT) these errors are reduced to just 0.2% and 0.05%.

4 Results

4.1 Comparison of modelled and observed F - UT patterns

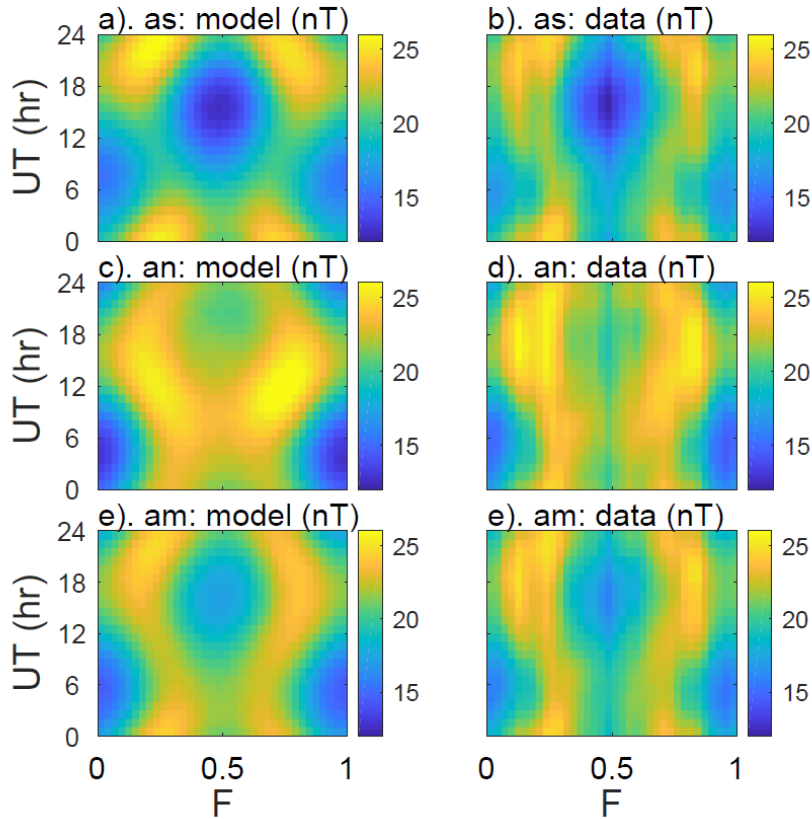


Figure 3. F - UT plots of: (top row) the southern hemisphere as index; (middle row) the northern hemisphere an index; and (bottom row) the global index $am = (an + as)/2$. The left hand column shows the model predictions, the right hand column shows observations from 1959-2019, inclusive.

Figure 3 shows that the modelled F - UT patterns match the observed ones very closely. The value of the one free fit parameter c_{MP} used in Figure 2 is 0.27, derived using the Nelder-Mead search method to find the minimum r.m.s. deviation between modelled (am_m) and mean observed am for the 864 F - UT bins used. The largest disagreement is for an for which the predicted peak in the UT variation at both equinoxes is near 13 hrs whereas in an data it is near 16 hrs. This almost certainly arises from the closeness of the northern geomagnetic dip pole from the rotation pole in recent decades (Thébault, et al., 2015) which makes it likely that the eccentric dipole fit to the field is underestimating how far the longitude separation of the two poles has fallen from 180° .

4.1 UT variations of average values and large event occurrence

This model predicts that the F - UT pattern will vary slowly over time as the geomagnetic axial poles migrate, but also will vary with the average level of the transpolar voltage and hence of the am index. To investigate this we here break the am data into three 20-year intervals, 1960-1979, 1980-1999 and 2000-2019 for which average am values are 21, 25 and 17 nT

(corresponding to $\Phi_{cf} \sim 39, 43$ and 34 kV) and compute $[V_X]_{NP}$ and $[V_X]_{SP}$ for the pole locations at the middle of each interval.

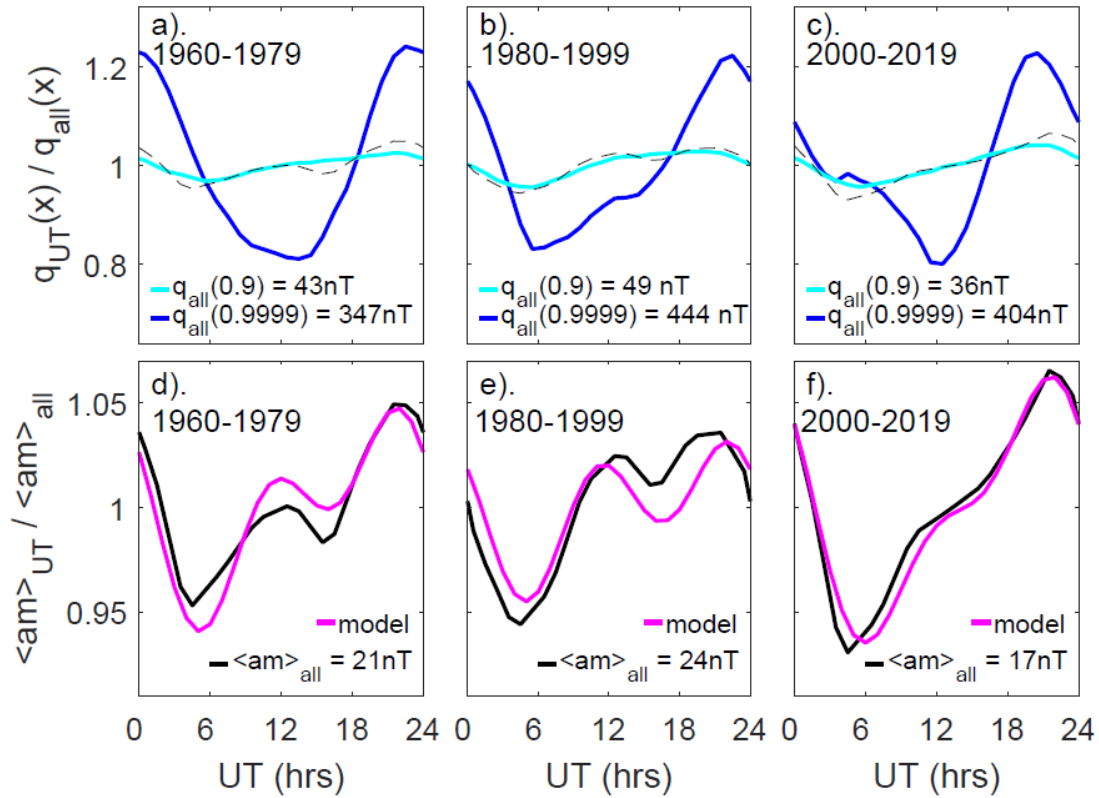


Figure 4. Universal time variations averaged over all F for: (a) and (d) 1960-1979; (b) and (e) 1980-1999; and (c) and (f) 2000-2019. The top panels show the UT variation in the 90% quantile of the distribution of am values ($q(0.9)$, cyan lines) and the 99.99% quantile ($q(0.9999)$, blue lines). The dashed lines show the variation for the mean am . Bottom panels show the variations for mean observed am (black lines) and modelled am , am_m (mauve lines).

The observed (black) and modelled (mauve) UT variations (averaged over all F) are shown in parts d-f of Figure 4. The higher activity levels for 1980-1999 mean that the pole motions are less important and the UT variation is dominated by the other two factors. For 2000-2019 the lower activity level means that the pole motions have a much greater effect. For 1960-1979 the effect is a more-even mix of the two. Parts a-c of Figure 3 compare the UT variations in average fields (reproduced as dashed black lines) with the occurrence of large geomagnetic storms giving the 90% quantile of the distribution of 3-hourly am ($q(0.9)$, cyan lines) and the 99.99% quantile ($q(0.9999)$, blue lines): it can be seen that, despite their rarity, even the latter are showing UT variation consistent with the effect of pole motions that have been introduced here for the first time.

5 Discussion and Conclusions

We have shown how pole motions in the sunward/antisunward direction introduce a *UT* variation into hemispheric geomagnetic activity that explains observed variations when combined with the R-M forcing effect and the effect of solar wind dynamic pressure in squeezing the near-Earth tail, an effect that varies with dipole tilt angle. This *UT* effect is significant for the forecasting and mitigation of space weather effects because the largest geomagnetic disturbances occur around midnight magnetic local time ($MLT = 0$ hrs) and hence the *UT* effect means there will be a longitudinal dependence. For example, Moscow and Helsinki are at $MLT = 0$ at around 21:46 and 22:29 *UT*, respectively, when the *UT* variation in storm occurrence peaks. The equivalent *UT*s for London and Cape Town are 00:04 and 23:38 when occurrence is only a little lower, but for New York and Buenos Aires it is 04:43 and 04:41 when it is considerably lower. When geomagnetic activity is high, the main feature is the minimum at 06 *UT* caused by the tail squeezing effect (Figures 3b and 3e) which Figure 1e shows to mainly occur around the December solstice. Hence, for example, disruption to power distribution networks (e.g., Hübert et al., 2020) in winter should be less likely in central in the mid-west of North America than, for example in Eurasia. Note that the effect identified in this paper depends of the axial magnetic pole locations that are now moving faster than at any time since observations began and empirical climatologies of space weather phenomena may need to allow for this.

Acknowledgments, Samples, and Data

The authors have no conflicts of interest in this work. They are grateful to the staff of the International Service of Geomagnetic Indices (ISGI), France and collaborating institutes for the compilation and data basing of the *am* indices which were downloaded from http://isgi.unistra.fr/data_download.php and to the staff of the Space Physics Data Facility (SPDF) at NASA's Goddard Space Flight Center for the Omni composite of interplanetary observations (made available by SPDF from https://omniweb.gsfc.nasa.gov/ow_min.html). The work of ML, LAB, CJS and MJO at University of Reading supported by the SWIGS NERC Directed Highlight Topic Grant number NE/P016928/1/ and by STFC consolidated grant number ST/M000885/1. The work of AWPT at BGS is also supported by SWIGS. Funding for KAW at University of Saskatchewan was provided by the Canadian Foundation for Innovation (CFI), the Province of Saskatchewan, and a Discovery Grant from the Natural Sciences and Engineering Research Council (NSERC) of Canada. Initial work by KAW for this paper was carried out at University of Reading on sabbatical leave from University of Saskatchewan. The work of OC at École et Observatoire des Sciences de la Terre (EOST) is supported by CNES, France. CH is supported on a NERC PhD studentship as part of the SCENARIO Doctoral Training Partnership.

References

- Bartels, J. (1925), Eine universelle Tagsperiode der erdmagnetischen Aktivität, *Meteorol. Z.*, 42, 147-152.
- Berthelier, A. (1976), Influence of the polarity of the interplanetary magnetic field on the annual and the diurnal variations of magnetic activity. *J. Geophys. Res.*, 81(25), 4546-4552. doi: 10.1029/ja081i025p04546

- Broun, J.A. (1848), Observations in magnetism and meteorology made at Makerstoun in Scotland. *Trans R. Soc. Edinburgh*, 18, 401–402
- Caan, M.N., McPherron, R.L. & Russell C.T. (1973), Solar wind and substorm-related changes in the lobes of the geomagnetic tail. *J. Geophys. Res.*, 78(34), 8087 – 8096. doi:10.1029/ja078i034p08087.
- Chambodut, A., et al. (2013), The K-derived MLT sector geomagnetic indices, *Geophys. Res. Lett.*, 40, 4808-4812. doi:10.1002/grl.50947
- Cliver, E.W., Kamide, Y., & Ling, A.G. (2000), Mountains versus valleys: Semiannual variation of geomagnetic activity. *J. Geophys. Res.*, 105, 2413– 2424. doi:10.1029/1999JA900439
- Cowley, S.W.H. & Lockwood, M. (1992), Excitation and decay of solar-wind driven flows in the magnetosphere-ionosphere system, *Annales Geophys.*, 10, 103-115.
- Finch, I.D., Lockwood, M., and Rouillard A.P. (2008), The effects of solar wind magnetosphere coupling recorded at different geomagnetic latitudes: separation of directly-driven and storage/release systems. *Geophys. Res. Lett.*, 35, L21105. doi:10.1029/2008GL035399
- Hapgood, M.A. (1992), Space physics coordinate transformations: A user guide. *Planet Space Sci.*, 40 (5), 711-717. doi:10.1016/0032-0633(92)90012-d
- Hübner, J. et al. (2020), Differential magnetometer measurements of geomagnetically induced currents in a complex high voltage network, *Space Weather*, 18, e2019SW002421. doi: 10.1029/2019SW002421
- Ieda, A., et al. (2014), Approximate forms of daytime ionospheric conductance, *J. Geophys. Res. Space Physics*, 119, 10,397–10,415. doi:10.1002/2014JA020665.
- Kabin, K. et al. (2004), Open-closed field line boundary position: A parametric study using an MHD model, *J. Geophys. Res.*, 109, A05222. doi:10.1029/2003JA010168.
- Koochak, Z. & Fraser-Smith, A.C. (2017), An update on the centered and eccentric geomagnetic dipoles and their poles for the years 1980–2015, *Earth and Space Science*, 4, 626–636. doi: 10.1002/2017EA000280
- Lin, R.L. et al. (2010), A three-dimensional asymmetric magnetopause model, *J. Geophys. Res.*, 115, A04207. doi:10.1029/2009JA014235
- Lockwood, M. (2013), Reconstruction and Prediction of Variations in the Open Solar Magnetic Flux and Interplanetary Conditions. *Living Reviews in Solar Physics*, 10, 4. doi: 10.12942/lrsp-2013-4
- Lockwood, M. (2019), Does adding solar wind Poynting flux improve the optimum solar wind-magnetosphere coupling function? *J. Geophys. Res. (Space Physics)*, 124 (7), 5498-5515, doi: 10.1029/2019JA026639.
- Lockwood, M. & Cowley, S.W.H. (1992), Ionospheric Convection and the substorm cycle, in “*Substorms I, Proceedings of the First International Conference on Substorms, ICS-I*”, ed. C. Mattock, ESA-SP-335: 99-109. European Space Agency Publications, Noordwijk, The Netherlands
- Lockwood, M. & Morley, S.E. (2004), A numerical model of the ionospheric signatures of time-varying magnetic reconnection: I. Ionospheric convection. *Annales Geophys.*, 22, 73-91. doi:10.5194/angeo-22-73-2004.
- Lockwood, M. et al. (2019a) The development of a space climatology: 1. Solar-wind magnetosphere coupling as a function of timescale and the effect of data gaps, *Space Weather*, 17, 133-156. doi: 10.1029/2018SW001856
- Lockwood, M (2019b) Time-of-day / time-of-year response functions of planetary geomagnetic indices. *J. Space Weather Space Clim.*, 9, A20. doi: 10.1051/swsc/2019017

Lockwood, M, et al. (2020a), Semi-annual, annual and Universal Time variations in the magnetosphere and in geomagnetic activity: 1. Geomagnetic data. *J. Space Weather Space Clim.*, 10, 23. doi:10.1051/swsc/2020023

Lockwood, M., et al. (2020b); Semi-annual, annual and Universal Time variations in the magnetosphere and in geomagnetic activity: 2. Response to solar wind power input and relationships with solar wind dynamic pressure and magnetospheric flux transport, *J. Space Weather Space Clim.*, 10, 30. doi:10.1051/swsc/2020033

Mayaud, P.-N. (1980), Derivation, Meaning and Use of Geomagnetic Indices, *Geophysical Monograph*, 22, American Geophysical Union, Washington, DC. doi:10.1029/GM022

McIntosh, D.H. (1959), On the annual variation of magnetic disturbance, *Philos. Trans. R. Soc. Lond., A*, 251, 525-552. doi:10.1098/rsta.1959.0010

Newell, P.T. & Meng, C.-I. (1989), Dipole Tilt Angle Effect on the Latitude of the Cusp and Cleft/Low-Latitude Boundary Layer, *J. Geophys. Res.*, 94, 6949–6953. doi:10.1029/ja094ia06p06949

Russell, C.T. & McPherron, R.L. (1973), Semiannual variation of geomagnetic activity, *J. Geophys. Res.*, 78, 82-108. doi:10.1029/JA078i001p00092

Stubbs, T.J. et al (2005), Simultaneous observations of the auroral ovals in both hemispheres under varying conditions. *Geophys. Res. Lett.*, 32, L03103. doi:10.1029/2004GL021199

Thébault, E. et al. (2015), International Geomagnetic Reference Field: the 12th generation. *Earth, Planets and Space*, 67, 79. doi:10.1186/s40623-015-0228-9

Tsyganenko, N.A. (2019), Secular drift of the auroral ovals: How fast do they actually move? *Geophys. Res. Lett.*, 46, 3017–3023. doi:10.1029/2019GL082159

Supplementary Materials for the paper

Universal Time Variations in Space Weather

M. Lockwood, M.J. Owens, C. Haines, L.A. Barnard, C.J. Scott, A. Chambodut, K.A. McWilliams and A.W.P. Thomson

Submitted to Geophysical Research Letters

Abstract. We here present details of some of the factors used in the main publication and give polynomial fits that are used in the production of the modelled $F-UT$ patterns of geomagnetic activity indices presented.

Contents:

- (i). Estimation of Power input into the magnetosphere**
- (ii). Time-of-day/time-of-year pattern plots**
- (iii) Calculation of the hemispheric conductivity factors, $P_{\Sigma N}$ and $P_{\Sigma S}$**
- (iv). Eccentric dipole axial pole locations and velocities in the GSEQ frame**
- (v). The pole motion factors P_{PM}**
- (vi). Russell-McPherron factor P_{RM}**
- (vii). Dipole tilt angle, ψ**
- (viii). The tail squeezing factor $P_{\psi}(\psi)$**

(i). Estimation of Power input into the magnetosphere

We use 1-minute data on the solar wind and interplanetary magnetic field, available from 1980 onwards as the Omni2 dataset from the Space Physics Data Facility (SPDF) at NASA's Goddard Space Flight Center: https://omniweb.gsfc.nasa.gov/ow_min.html, to estimate the power input into the magnetosphere using the equation (see Lockwood, 2019 and references therein:

$$P_{\alpha} = \left(\pi k_2 k_1^2 M_E^{2/3} \mu_0^{-1/3} \right) m_{sw}^{(2/3-\alpha)} N_{sw}^{(2/3-\alpha)} V_{sw}^{(7/3-2\alpha)} B^{2\alpha} \sin^4(\theta/2) \quad (1)$$

where k_1 and k_2 are constants; M_E is the magnetic moment of the Earth which can be computed for a given time using the IGRF-15 Model (Thébault et al., 2015), μ_0 is the permeability of free space (the magnetic constant); m_{sw} is the mean ion mass, N_{sw} the number density and V_{sw} is the speed of the solar wind at Earth; B is the near-Earth Interplanetary Magnetic Field (IMF) and θ is the clock angle the IMF makes with the Z-

direction of the Geocentric Solar Magnetospheric frame of reference; α is called the coupling exponent and is the one free fit parameter. We use the optimum value of $\alpha = 0.44$ that yields the maximum correlations with the am index: Lockwood (2019) shows that these are 0.79 for the 3-hourly basic resolution of the am data, 0.91 for daily means, 0.93 for Carrington rotation means and 0.98 for annual means (all of which are highly statistically significant giving p values for the null hypothesis of less than 0.0001). The mean ion mass m_{SW} generally only available at hourly or 15 second resolution and are linearly interpolated to the 1-minute resolution, a procedure that readily meets the 5% error limit adopted in tests using the available 15-second resolution data. The 1-minute P_α data are then averaged into hourly intervals. Data gaps are handled using the criteria for the required number of samples for each parameter that ensures that the error in hourly P_α value is below 5%. These criteria were established by Lockwood *et al* (2018) by introducing synthetic data gaps into continuous data. Hourly intervals not meeting these criteria in all parameters were treated as data gaps in the P_α data series.

(ii). Time-of-day/time-of-year pattern plots

The patterns with fraction of a calendar year (F) and Universal Time (UT) are generated by averaging the hourly data for each UT in 36 equal width bins of F (each just over 10 days in width). This yields 864 bins and we applying a 2-dimensional 1-3-1 triangular weighting smooth in both the F and UT dimensions. For the observations the am , an , and as data are linearly interpolated to hourly values from the 3-hourly indices using linear interpolation.

(iii). Calculation of the hemispheric conductivity factors, $P_{\Sigma N}$ and $P_{\Sigma S}$

In theory, conductivities could be evaluated for every location in the polar regions using empirical relationships for a given solar zenith angle, χ . However this leaves the problem as to which locations most influence the an and as hemispheric sub-indices (and hence $am = (an + as)/2$): for example, what is the dependence on conductivity in the auroral oval compared to that over the observing magnetometer? Hence we take an empirical approach using means over several days of the deviations of an and as from am that average out the UT variations and studying the dependence of $\Delta an = (an - am)$ and $\Delta as = (as - am)$ with F and compare with the corresponding variations of the mean dipole tilt angle, ψ . Figure S1 shows the results.

The best 4th-order polynomial fit for the northern hemisphere index an is

$$\begin{aligned} \Delta an/an &= 1.064 \times 10^{-8} \psi(F)^4 + 2.840 \times 10^{-6} \psi(F)^3 \\ &+ 1.910 \times 10^{-5} \psi(F)^2 + 1.695 \times 10^{-3} \psi(F) - 0.884 \times 10^{-2} \end{aligned}$$

The factor $P_{\Sigma N}$ converts an ideal value of an (an_{cc}) into what we actually observe (an), such that

$$an = P_{\Sigma N} \times an_{cc}$$

If, for a first order correction we take am to be a good estimate of an_{cc} on the approximately 10-day timescales considered in Figure S1, then $an_{cc} = an - \Delta an = an/P_{\Sigma N}$

hence the northern hemisphere conductivity factor is $P_{\Sigma N} = (1 - \Delta an/an)^{-1}$ and likewise that for the southern hemisphere, $P_{\Sigma S} = (1 - \Delta as/as)^{-1}$.

The best 4th-order polynomial fit for the southern hemisphere index as is

$$\begin{aligned} \Delta as/as &= -0.948 \times 10^{-8} \psi(F)^4 - 3.137 \times 10^{-6} \psi(F)^3 \\ &- 2.238 \times 10^{-5} \psi(F)^2 - 1.138 \times 10^{-3} \psi(F) - 0.988 \times 10^{-2} \end{aligned}$$

The corrected indices, $an_{cc} = an/P_{\Sigma N}$, $as_{cc} = as/P_{\Sigma S}$ and $am_{cc} = (an_{cc} + as_{cc})/2$ are shown in Figure S1b. Note that the corrections make an_{cc} and as_{cc} very similar indeed. Note also that the resulting am_{cc} is not exactly the same as am : the semi-annual variation in am_{cc} is slightly larger in amplitude and there is different structure around the peaks (which is also seen in both an_{cc} and as_{cc}). This indicates that the conductivity effects in the two hemisphere do not exactly cancel in am . The residuals for the polynomial fits give a percentage root mean square (r.m.s.) error in $P_{\Sigma N}$ and $P_{\Sigma S}$ of just 0.21%.

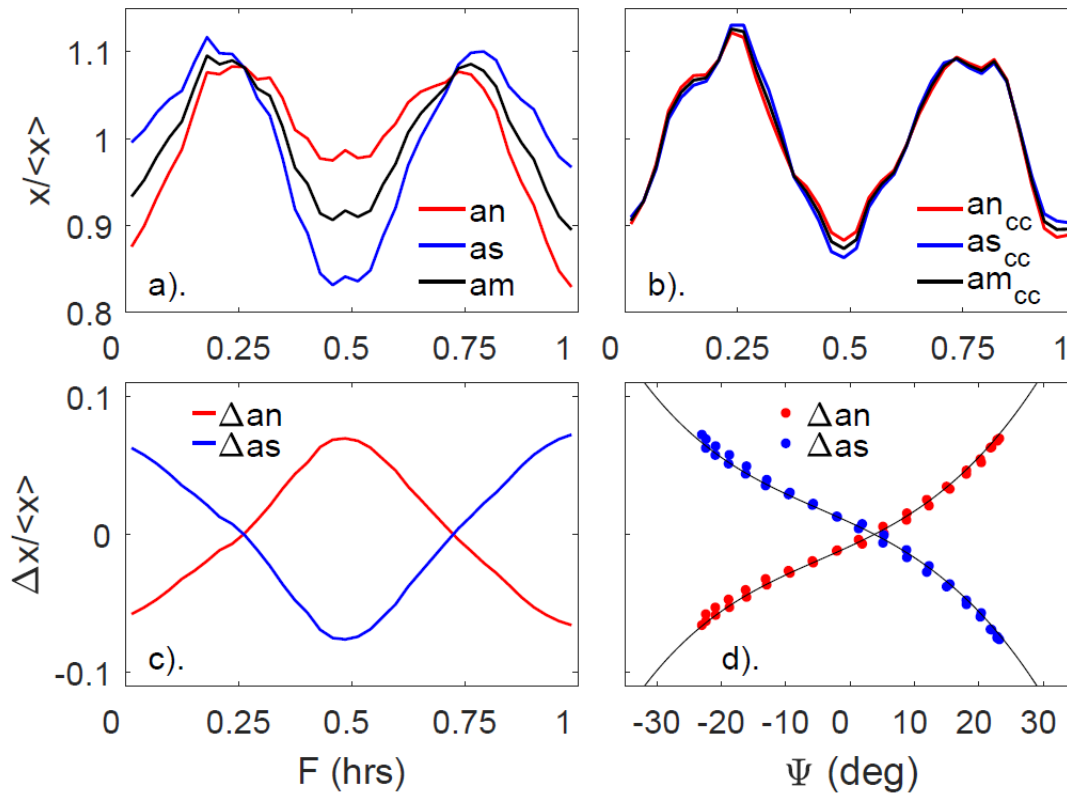


Figure S1. (a) The observed variations of the geomagnetic indices with fraction of year, shown as a fraction of their overall mean: (red) $an(F)/\langle an \rangle_{all}$; (blue) $as(F)/\langle as \rangle_{all}$; and (black) $am(F)/\langle am \rangle_{all}$. (b) The variations after correction for conductivity effects (using the factors derived): (red) $an_{cc}(F)/\langle an_{cc} \rangle_{all}$; (blue) $as_{cc}(F)/\langle as_{cc} \rangle_{all}$; and (black) $am_{cc}(F)/\langle am_{cc} \rangle_{all}$. The deviations of an and as from am , (red) $\Delta an = an - am$, (blue) $\Delta as = as - am$, which for the 36 bins in F (≈ 10 -day timescale) are taken to be due to conductivity effects alone. (d) The variations of (red points) Δan and (blue points) Δas as a function of the mean dipole tilt angle, ψ for the same F -UT. The black lines are 4th-order polynomial fits to the points.

(iv). Eccentric dipole axial pole locations and velocities in the GSEQ frame

The eccentric dipole axis \vec{M} (a dipole axis not constrained to pass through the Earth's centre) was taken from the work of *Koochak and Fraser-Smith (2017)* using the coefficients for the two axial pole locations that were linearly interpolated from their tabulated values to the middle date of the *am* data interval under consideration. The location and motion of the eccentric axial poles in geographic coordinates into the GSEQ frame using the CXFORM Coordinate transformation package originally written by Ed Santiago of Los Alamos National Laboratory and Ryan Boller of NASA's Goddard Space Flight Centre and re-programmed for Matlab by Patrik Forssén (SatStar Ltd & Karlstad University) in 2017, available from https://spdf.sci.gsfc.nasa.gov/pub/software/old/selected_software_from_nssdc/coordinate_transform/#Mi. This software package is based on the equations by Mike Hapgood of RAL Space, Rutherford Appleton Laboratory (*Hapgood, 1992*).

GSEQ locations of the poles at an altitude of 800 km (in the topside ionosphere) were computed at the 36 values of *F* and for three times around the 24 hourly *UT* values, these times being shifted by -1min , 0 and $+1\text{min}$ from each *UT* value and the velocities $[V_X]_{NP}$ and $[V_X]_{SP}$ computed from the difference in the *X* coordinates for the -1min , and $+1\text{min}$ cases.

(v). The pole motion factors P_{PM}

The sunward motion (in the $+X$ direction) in the GSEQ frame of the northern axial pole at speed $[V_X]_{NP}$ generates a modulation to the northern ionospheric cap transpolar voltage in that frame of

$$\Delta\Phi_{cfN} = d \times \langle B_{iYZ} \rangle \times [V_X]_{NP}$$

where d is the polar cap diameter and $\langle B_{iYZ} \rangle$ is the ionospheric magnetic field normal to the *X* direction. The average effect for the two polar caps is then

$$\Delta\Phi_{cf} = \frac{\Delta\Phi_{cfN} + \Delta\Phi_{cfS}}{2} = d \times \langle B_{iYZ} \rangle \times \frac{([V_X]_{NP} + [V_X]_{SP})}{2}$$

$$\text{and } P_{PM}(UT) = \Delta\Phi_{cf} / \Phi_{cf}$$

where we compute Φ_{cf} for a given *am* from the regression equation given by equation (A4) in Appendix A of *Lockwood et al. (2020b)*.

$$\Phi_{cf} = (6.68 \times 10^{-5})am^3 - (1.66 \times 10^{-2})am^2 + 1.89am + 6.17$$

(vi). Russell-McPherron factor P_{RM}

The CXFORM Coordinate transformation package was also used to compute the GSEQ to GSM transformation of unit IMF vectors in the $+Y$ and $-Y$ directions of GSEQ and give the IMF clock angle θ and hence the Russell-McPherron predictions of the $\sin^4(\theta/2)$ IMF orientation factor in P_α and hence the factor $P_{RM}(F, UT)$. Note that in the original paper, Russell and McPherron (1973) used a half-wave rectified southward component IMF orientation factor (B_S/B) whereas we employ $\sin^4(\theta/2)$: these two have been compared and discussed by Lockwood et al. (2020b).

(vii). Dipole tilt angle, ψ

The dipole tilt angle was computed as a function of F and UT , being the angle between \vec{M} and the \vec{S} , the geocentric position vector of the subsolar point, computed using the SUBSOL routine of the LOWTRAN7 Sun and Moon Models Matlab package generated by Noah of the US Air Force Geophysics Laboratory in 2019 and available from https://www.mathworks.com/matlabcentral/fileexchange/71203-lowtran7-sun-and-moon-models?s_tid=FX_rc1_behav.

(viii). The tail squeezing factor $P_\psi(\psi)$

This factor was modelled by *Lockwood et al. (2020b;c)* using the asymmetric magnetopause location model of *Lin et al. (2017)* by assuming that the tail is in equilibrium with a solar wind of dynamic pressure p_{sw} . Figure S2. shows the variations with tilt angle derived.

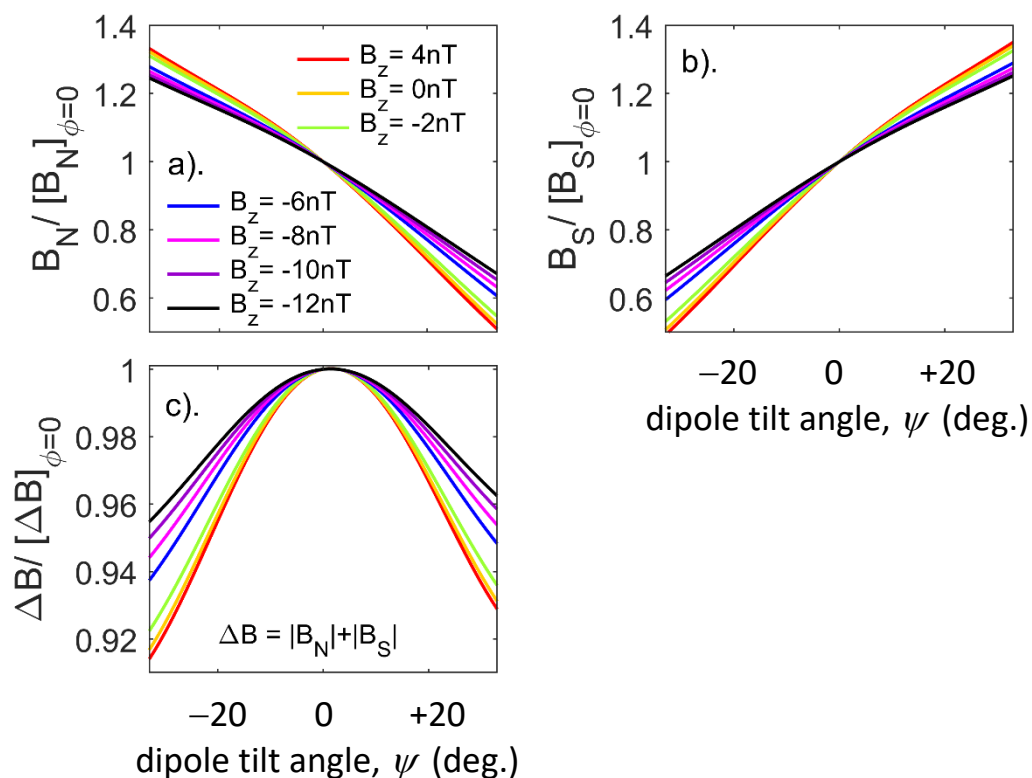


Figure S2. (Top panels) The modelled maximum lobe field along the bisector of the tail hinge angle, evaluated from the magnetopause location and magnetosheath pressure for the Newtonian approximation by assuming the tail is in equilibrium, and shown as a function of the dipole tilt angle ψ for various values of the IMF B_z and the mode values of the distributions of solar wind static and dynamic pressures for 1980-2018 of $p_{st} = 0.015$ nPa and $p_{sw} = 1.50$ nPa. (a) shows the field in the northern lobe, B_N , (b) shows that in the southern lobe, B_S , both as a ratio of their values for $\psi = 0$. The fall in B_N with increasing ψ is mirrored by a rise in B_S , but not quite exactly: this can be seen in part (c) that shows the magnetic shear across the hinge in the current sheet $\Delta B = |B_N| + |B_S|$ which is proportional to the current per unit length in the cross-tail current sheet (again plotted values are normalized to the value for $\psi = 0$, $[\Delta B]_{\phi=0}$). In all panels the various colors are for different IMF $[B_z]_{GSM}$ inputs to the magnetopause model that vary from +4nT (red) to -12nT (black). It can be seen that ΔB is

largest for $\psi = 0$ but is also larger for large positive ψ than large negative ψ . This is a consequence of the hemispheric asymmetry in the magnetopause model.

A 4th order polynomial that fits (with scaling) all the variations of ΔB in Figure S2c that is accurate to within an r.m.s. error of 0.02% is

$$P_{\psi\Delta B}(\psi) = 3.645 \times 10^{-8} \psi^4 - 1.059 \times 10^{-7} \psi^3 - 1.115 \times 10^{-4} \psi^2 + 4.768 \times 10^{-4} \psi + 1$$

Lockwood et al. (2020b) show that the equinoctial pattern in the *am* index increases linearly in amplitude with solar wind dynamic pressure and fitting the above functional form $P_{\psi\Delta B}(\psi)$ to the pattern amplitude they find for *am* observations for the mode value of p_{SW} of 1.50 nPa yields

$$P_{\psi}(\psi) = 1 + 3.80 \times \{P_{\psi\Delta B}(\psi) - 1\}$$